Chapter 3

Synthesized shot gathers from Valhall

SUMMARY

BP made available assive recordings from an array of 2300 four component receiver stations at the Valhall reservoir in the Norwegian North Sea from February 2004 and January 2005. Analysis of the raw hydrophone records shows that the bulk of the records do not yield obvious events. Hyperbolic events with water velocity are sometimes seen which are centered at the location of the platforms within the array. Also, there are occasionally noise trains in the raw data with an appearance of ringing, noisy shot gathers approximately 7 s long. These are also sourced from the production facilities at Valhall.

Simple correlation does not yield interpretable synthesized shot gathers from the raw data. Spectral whitening of the correlations reveals several interesting features. There are a few complete hyperbolas in the data that may correspond to the desired events analogous to active seismic data. Dominating the gathers however, is a single event from a source probably 40 km to the S. West of the array traveling at roughly 1450 m/s. The same event is present in both the 2004 and 2005 data. The inverted source location for the event is exactly over the Ardmore field in British waters, operated by Tuscan Energy (Scotland) Limited.

INTRODUCTION TO THE VALHALL ARRAY

BP, with partners Hess, Shell, and Total, provided approximately 43 hours of continuous passive seismic records from the permanent sensor installation above the Valhall reservoir in the Norwegian North Sea. Figure 6.1 is a map provided by the Norwegian Oil Directorate which shows the production infrastructure between the coasts of England and Norway with the many developments in the region. It is 630 km from the Southern tip of the Norway shown and the city of Teeside in England. The Valhall development is roughly in the center of the line connecting those two geographic points.

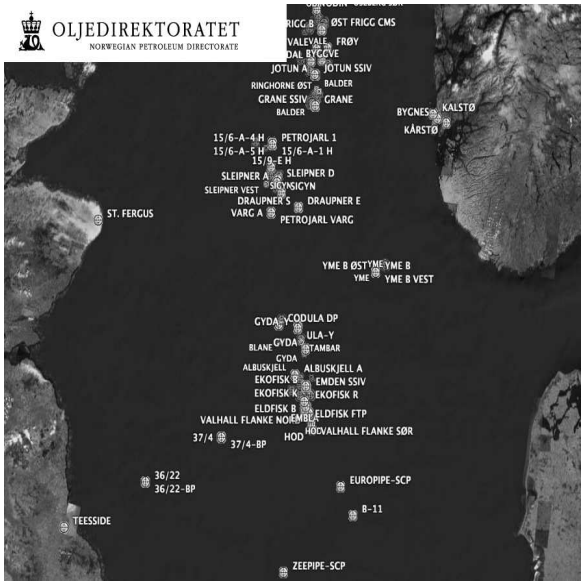

Figure 3.1: English, Norwegian, and Danish coasts surrounding the North Sea oil development area. The Valhall reservoir is in the South-central area of the map and only 20 km from English-controlled waters to the West, and Danish waters to the South. TimeShot-areamap [NR]

There are five surface structures (roughly over the center of the reservoir), and two wellhead platforms at the North and South ends of the NW-SE elongate elliptical reservoir (both roughly 6 km from the central platforms). The main fluid export pipeline runs NNW to the Ekofisk reservoir, about 30 km distant. Figure 3.2 shows the location of the 13 lines of OBC 4C geophones installed in the summer of 2003 to facilitate time-lapse imaging of the subsurface for production monitoring. The +9,000 sensors are permanently installed 1 m below the sea floor, in roughly 70 m of water. The array forms a roughly 4x11 km rectangle. Nominal inline spacing of receiver stations is 50 m, while the crossline separation is 300 m.

Approximately half-way down the North axis of Figure 3.2, the cables on the Western

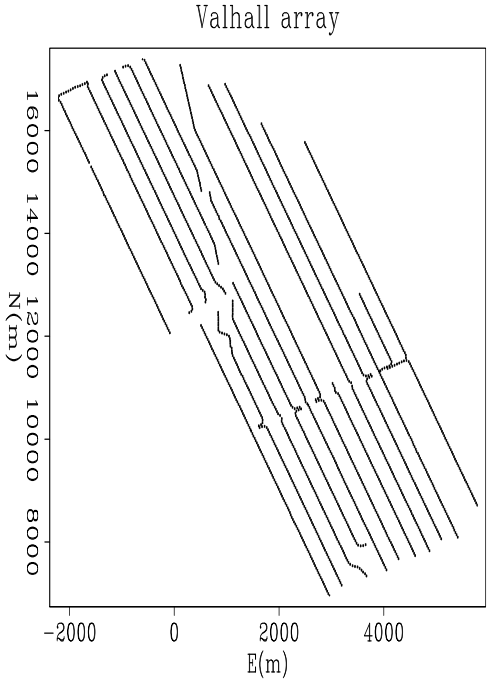

Figure 3.2: Valhall permanent subsea geophone array. Each station measures 4 components (4C) of the seismic wavefield: Pressure with a piezoelectric sensor, and three orthogonal velocities of ground displacement with coil-spring geophones. TimeShot-actg [NR]

side of the array are truncated. This is where the production facilities are located to which the instruments are telemetered. Also noticeable is the deviation of the ends of cables on the North side of lines 5-7 (E=1000 m) to the NNW. This is the corridor for the export lines to Ekofisk. Production facilities are continuously manned and operated, to include: Over 150 total well-bores into the reservoir section, current production of approximately 80,000 b/d oil and gas from 43 wells, water injection through (at least) 3 wells, generation of almost 80 MW of electric power with gas turbines, flow through the export lines, and the continual presence of multiple modes of transportation[1]. Valhall is located in a heavily developed area, within kilometers of developments in the English and Norwegian controlled waters and is about halfway between the two countries. Also important to the chalk oil trend of this part of the North Sea is the rate of subsidence associated with pressure withdrawal during production. In its first 15 years of production (to 1997), the sea-floor subsided 3.5 m at the crest of the reservoir structure (Gebara et al., 2000).

[1] www.npd.no/engelsk/

PASSIVE SEISMIC RECORDING

The passive recordings donated by BP are from 29 hours February 15, 2004 and 14 hours January 19, 2005. Of the former, some 7 hours was lost due to a failed disk-drive. The most likely teleseismic arrival recordable at the array, as determined by query of the National Earthquake Information Center event catalog[2], arrived approximately 5 hours after the last records available. Of the 2300 4C stations, this work uses the hydrophone measurement from each location. The data are sampled at 0.004 ms, and written as contiguous files between 12-20 s long. Figure 3.3 shows an example of the character of most of the data. The traces are balanced against each other, but are otherwise raw recordings. Scanning through a subset of the raw data, I was not able to identify clear events. Most of the raw data look like incoherent noise, but I found several interesting features that will be explored below.

Figure 3.4 shows a conspicuous noise-train in a section of raw data. The figure shows all of the traces within the array, progressing (roughly) North to South down each cable, and West to East across the cables. An inline section from a single cable contains roughly 220 traces, and a cross-line section contains only 11 traces on average. While there are no coherent events in the figure, a noise-train about 7 s long within the background chatter is reminiscent of a noisy shot-gather. The minimum travel time of the noise-train is at trace 650. This trace is located at the South end of the top half of the fourth receiver line. The various jogs and cable terminations of this region are associated with the surface facilities on location. Plotted over the data are circles corresponding to a direct arrival from the location of the platforms in the plane of the receivers. These were shifted to align with the top and bottom of the noise train. The velocity used to model this event is 1450 m/s. The fact that there is no velocity increase for the bottom of the envelope suggests that this feature does not contain reflections from the subsurface. Similar examples of this type of noise-train are periodically recognizable throughout data recordings. The source of the energy has a complex coda and a finite duration.

Figure 3.5 shows a time window when a crisp series of hyperbolic events is captured by the array. The top panel is the Eastern half of the array and the bottom is the Western half. The

[2] http://earthquake.usgs.gov/regional/neic/

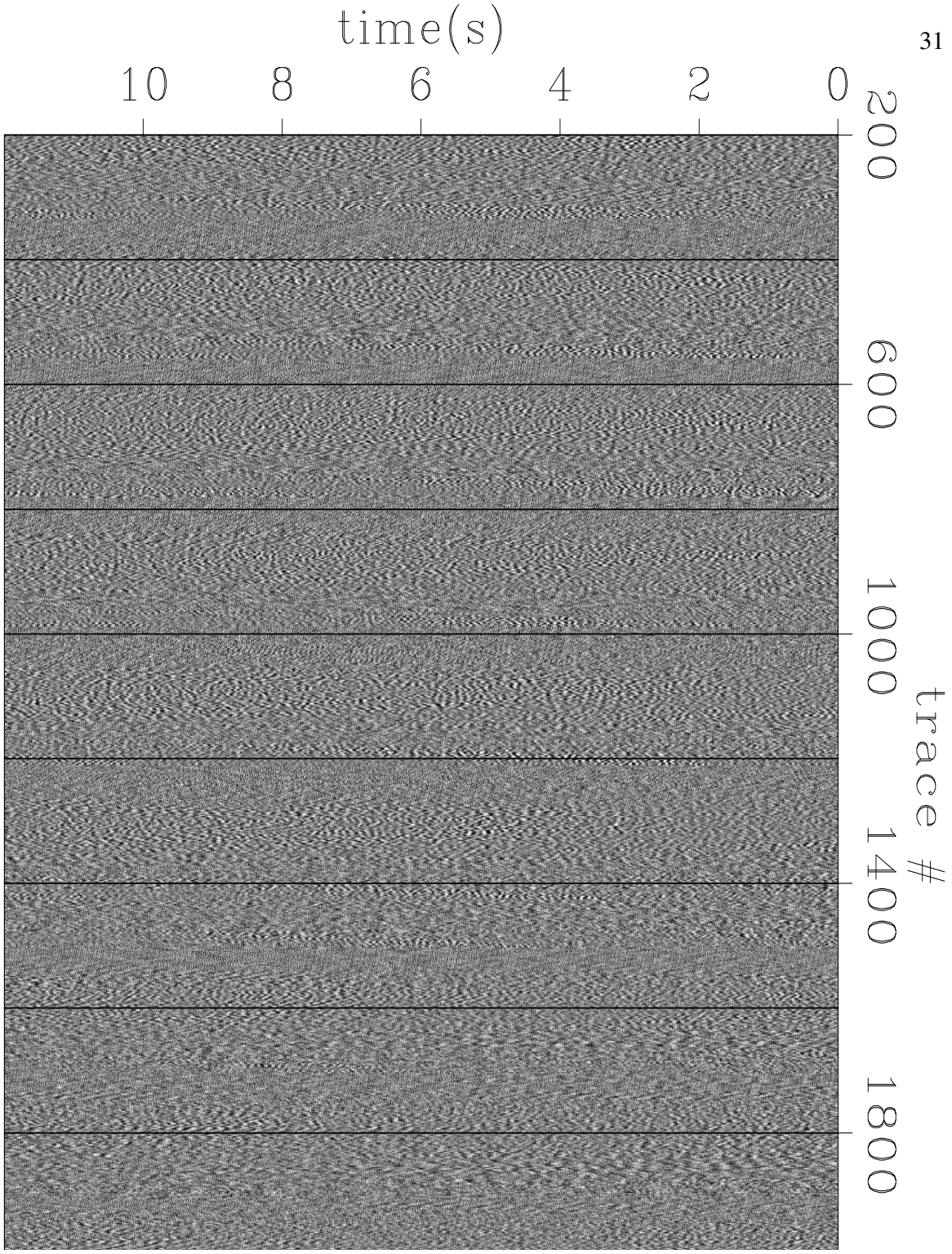

Figure 3.3: Twelve seconds of representative passive hydrophone data from February 16, 2004. Trace number increases from the top left to bottom right corners of the array shown in Figure 3.2. TimeShot-raw1 [ER]

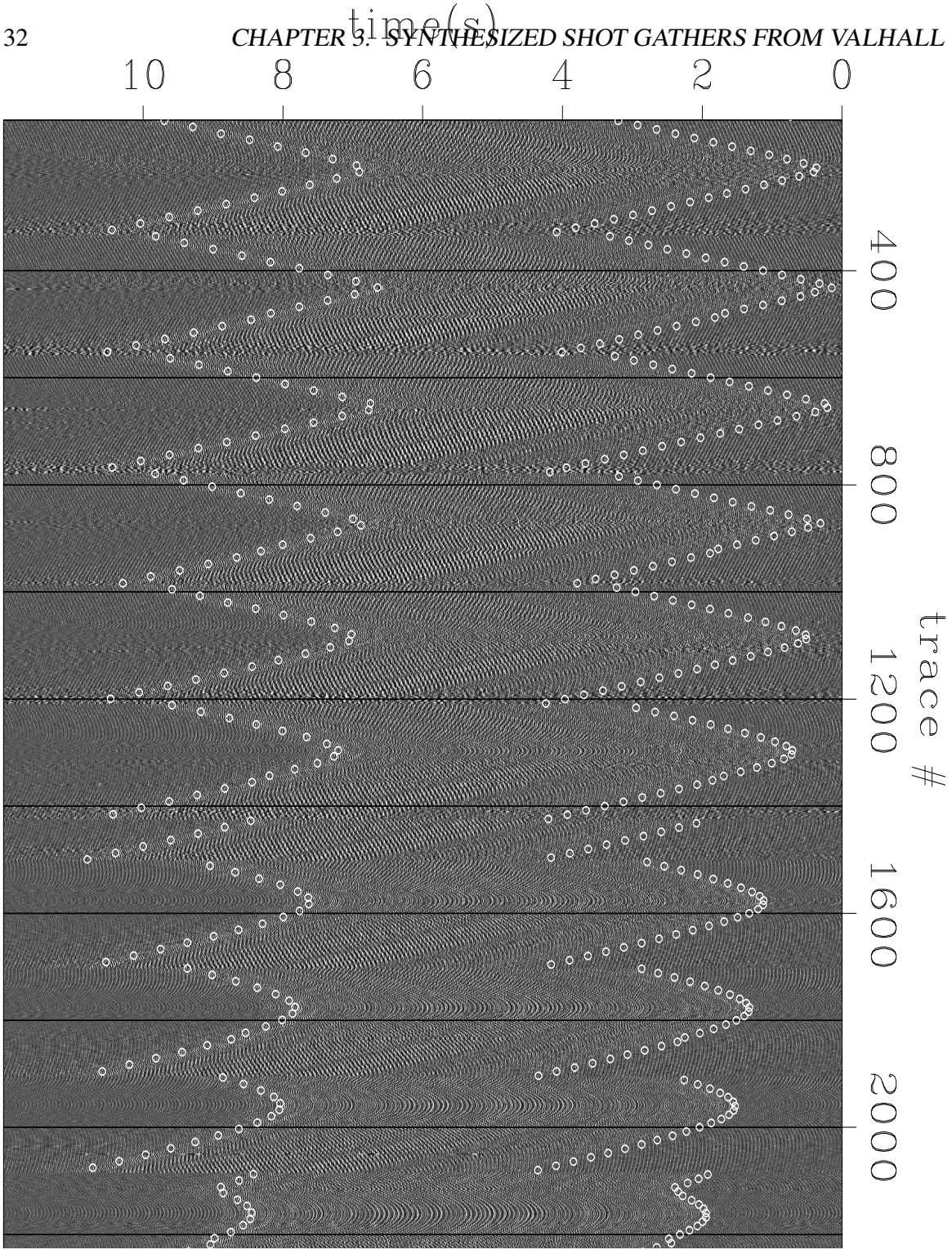

Figure 3.4: Raw data with a powerful noise train envelope. The 13 lines of the array show as the event is repeated and shifted over cross-line offset. Circles are co-planar direct arrivals from the center of the array traveling at 1450 m/s. TimeShot-raw2 [ER]

minimum traveltimes of the hyperbolas in the data decrease to the West in a similar fashion to the onset of the noise section in the previous figure. This suggests that the production facilities are again the source of the energy. The circles overlaying the data in Figure 3.5 show the kinematics of a a co-planar direct arrival from the large 'O' in Figure 3.6 (explained below) traveling at 1450 m/s. The modeled arrival times are plotted on every third trace to avoid clutter. However, even when plotting all picks in high resolution, the forward modeling clearly shows that the data are aliased at this slowness value over the center of the array where the event is not visible. Similar events are recognizable throughout the records, though this is a particularly clear example.

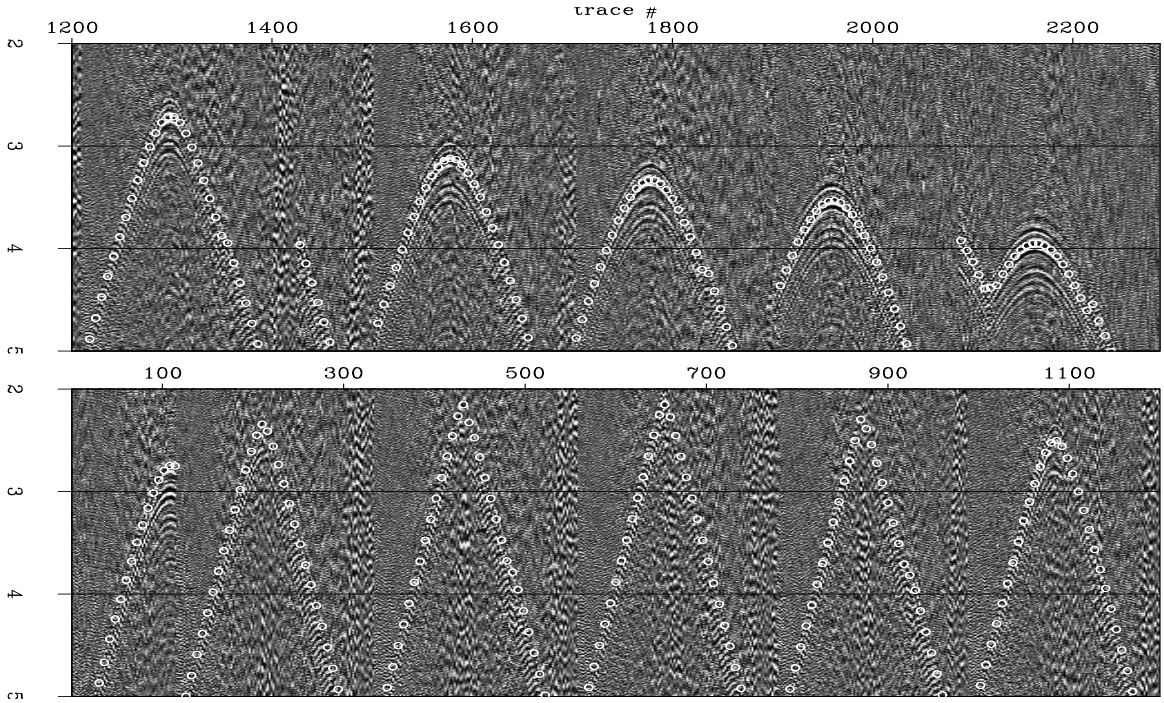

Figure 3.5: Raw data with a clear hyperbolic event annotated with the time calculated for a coplanar direct arrival from the array center traveling at 1450 m/s are. TimeShot-raw3ev [ER]

Figure 3.6 is a map of the array rotated to convenient field coordinates. The 'X' symbols mark the locations of the traces with minimum hyperbolic traveltimes that are obvious in the previous figures. The line containing the minimum traveltime picks shows no inline offset variation and includes the area around $y = 6250$ m, which is the location of the platforms

(presumably near the large 'O' symbol). This figure provided the inline coordinate for the picks plotted in Figures 3.4 & 3.5. The cross-line coordinate was deduced by matching the picks to the various observations. The four cables with circled receiver stations indicate a subset of the array used for later figures.

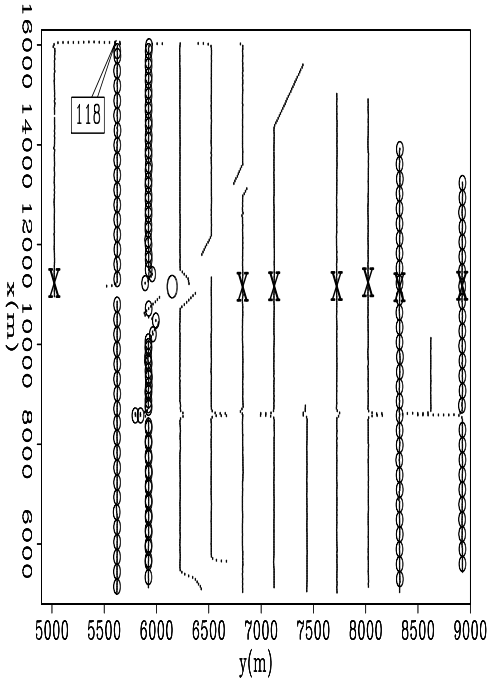

Figure 3.6: Receiver array in field coordinates. Marked with 'X' are the locations of traces with minimum traveltimes picked from the hyperbolas in Figure 3.5. Surface facilities are roughly at the large O. Trace 118 is the virtual source location for the synthesized gathers in Figures 3.7-3.14, 3.16 and the origin in the black line in Figure 3.18. Cables marked with circles indicate receiver locations used in Figures 3.10-3.14,3.16. TimeShot-minloc [ER]

CORRELATION

Following the theory from Wapenaar et al. (2004), the basic principle of time processing passively recorded seismic records to synthesize the kinematics of conventional shot gathers dictates that individual transmission wavefields should be correlated before summing the results. Because windowing individual arrivals from the +36 hours of passive data impractical (because of the large volume and the lack of identifiable events), it is impossible to honor equation 1.1 precisely by correlating traces within time windows when only a single event is active. I make the assumption that processing data in 12 second sections is a reasonable approximation to the requirement. The available data were divided into three sections for processing: one 13.5 hours, two 9 hours, and one 4.5 hours in duration. Sequential 12 s records within these

sections were correlated and the results stacked over the duration of the (hours long) section of the total data. Thus

$$\tilde{R}(\mathbf{x}_r, \mathbf{x}_s, \omega) = \sum_{\xi} T(\mathbf{x}_r, \omega, \xi) T^*(\mathbf{x}_s, \omega, \xi) \tag{3.1}$$

was calculated where ξ is the index of sequential 12 second windows of data.

Figure 3.7 shows correlations from one of the 9 hour sections of data. A trace from the NW corner (receiver 118 in Figure 3.6) was used to correlate all the other traces in the array. If the processing was perfect, the figure would show something equivalent to an off-end areal shot-gather. Energy to 60 Hz energy was used in the correlations, with cosine tapers beginning at 3 and 57 Hz. Unfortunately, the image, and the other similar ones, do not reveal anything of interest. Figure 3.8 plots the power spectrum of the sum of 100 traces from the gather in Figure 3.7. The power spectrum of the gathers produced from all four subsections of the raw data were very similar. Versions of the gathers (with all subsections of the raw data) bandpassed around and between the peaks in the plot of the spectrum made no increase in interpretability.

Spectral whitening by division of a trace in the frequency domain with its power produces remarkable results when compared to simple correlation. I produced gathers using the relation

$$\tilde{R}(\mathbf{x}_r, \mathbf{x}_s, \omega) = \sum_{\xi} \frac{T(\mathbf{x}_r, \omega, \xi) T^*(\mathbf{x}_s, \omega, \xi)}{|T(\mathbf{x}_r, \omega, \xi)\, T^*(\mathbf{x}_s, \omega, \xi)|}\,, \tag{3.2}$$

where the denominator is simply the complex absolute value of the numerator. The algorithm was very stable and showed no need to smooth the denominator as is common practice in similar deconvolutional efforts. In fact, smoothing the denominator across the trace axis produced large amounts of hard zero results. This can only be explained by large amplitude, uncorrelated energy on neighboring traces. Dividing a weak sample by a very strong neighbor will produce very small values. Smoothing across the frequency axis mixes early- and late-time energy, and therefore is not appropriate.

Figure 3.9 shows the same gather as in Figure 3.7 using the spectral whitening of equation 3.2. A very clear event is now apparent. Similar features can be seen upon close inspection

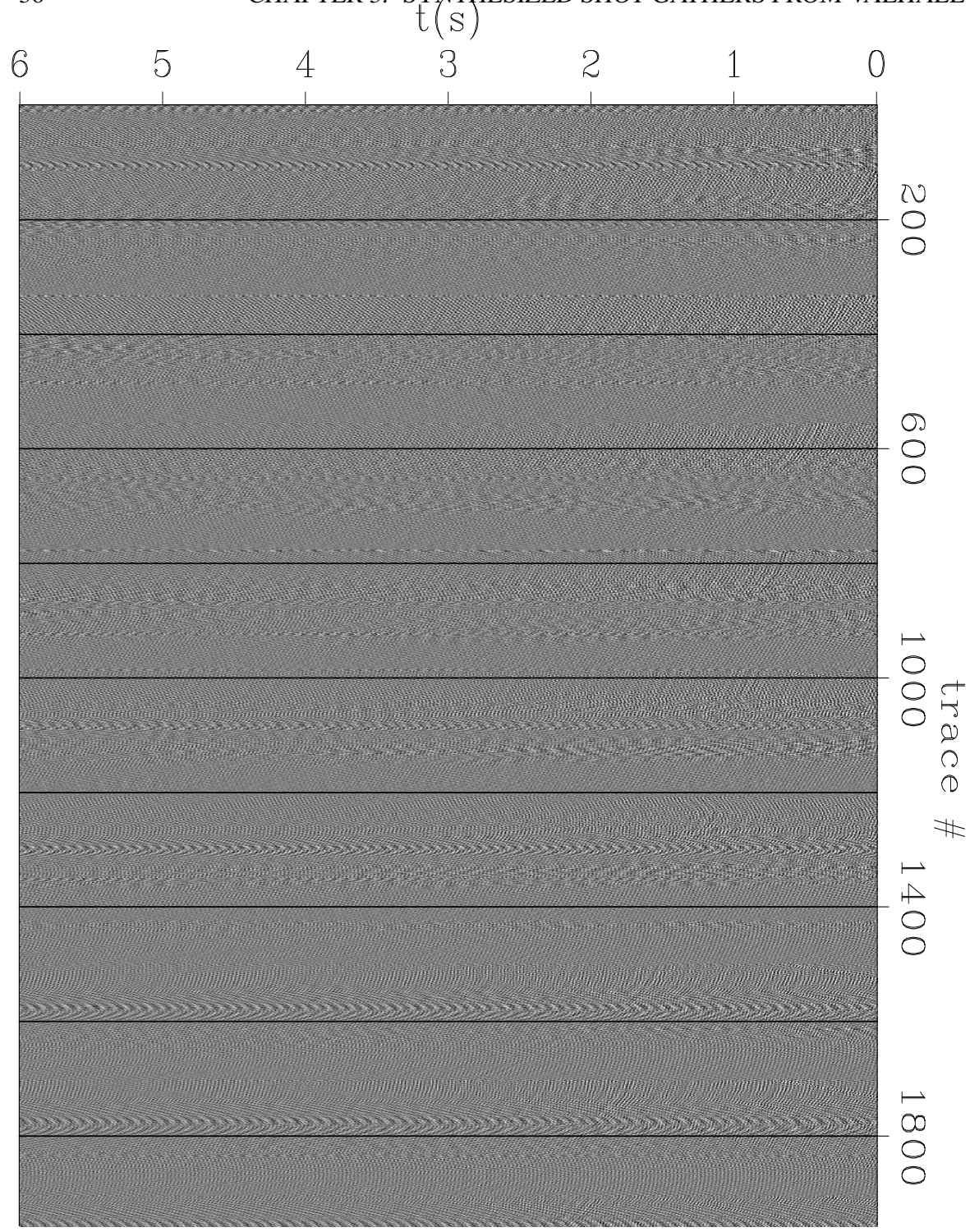

Figure 3.7: Correlated shot-gather with master trace from the left side of the panel. 0-60 Hz energy was used for the correlation performed in the frequency domain. TimeShot-cor [CR]

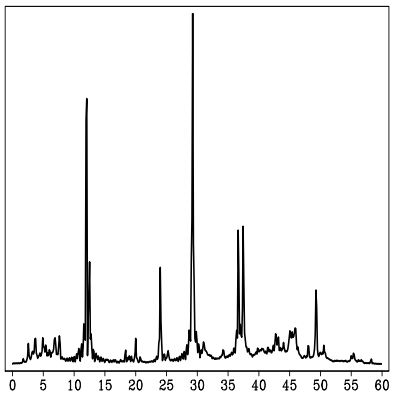

Figure 3.8: Power spectrum of the gathers in Figure 3.7. TimeShot-spec [CR]

of the correlated result after viewing the deconvolved gather. The various features of the obvious event in the gather reveal important features of the presumed source energy. The event is coherent across the entire 50 km^2 of the array and has reasonable bandwidth. The deconvolved gathers, produced with all subsections of the raw data, were bandpassed across the intervals between and surrounding the energy maximums in power spectrum, Figure 3.8, of the correlated gathers. No coherent energy was present at all through 8 Hz. Five versions from 9-40 Hz showed only minor differences, with the strong event equally well represented. After 42 Hz, the signal begins to diminish markedly, and no coherent energy is present at all after 52 Hz.

Events revealed by deconvolution processing, equation 3.2, in Figure 3.9 are hyperbolic. This indicates the event could be caused by any solution to the Eikonal equation. Possible solutions include the direct arrival of a buried source, or the reflection of a point source from a plane. No line contains the top of the hyperbola. This means that the source of the energy is not contained within the area of the array. The moveout of the event is monotonic to the South and East (in field coordinates). This indicates that the source must be to the North and West. Moveout is curve-linear in the inline direction, but very close to linear in the cross-line direction (white line over data in Figure 3.9). The line connecting the minimum traveltimes of the event on each cable deviates from straight only at the far right side. Notice from the map in Figure 3.6 that cross-line offset there is twice the normal spacing. Thes observations indicate that the array is close to the asymptote of the hyperbolic event in the cross-line direction, and nearer the hyperbola top in the inline direction. Therefore, the source is much closer to the array in the inline direction than the perpendicular direction. Given the true geographical

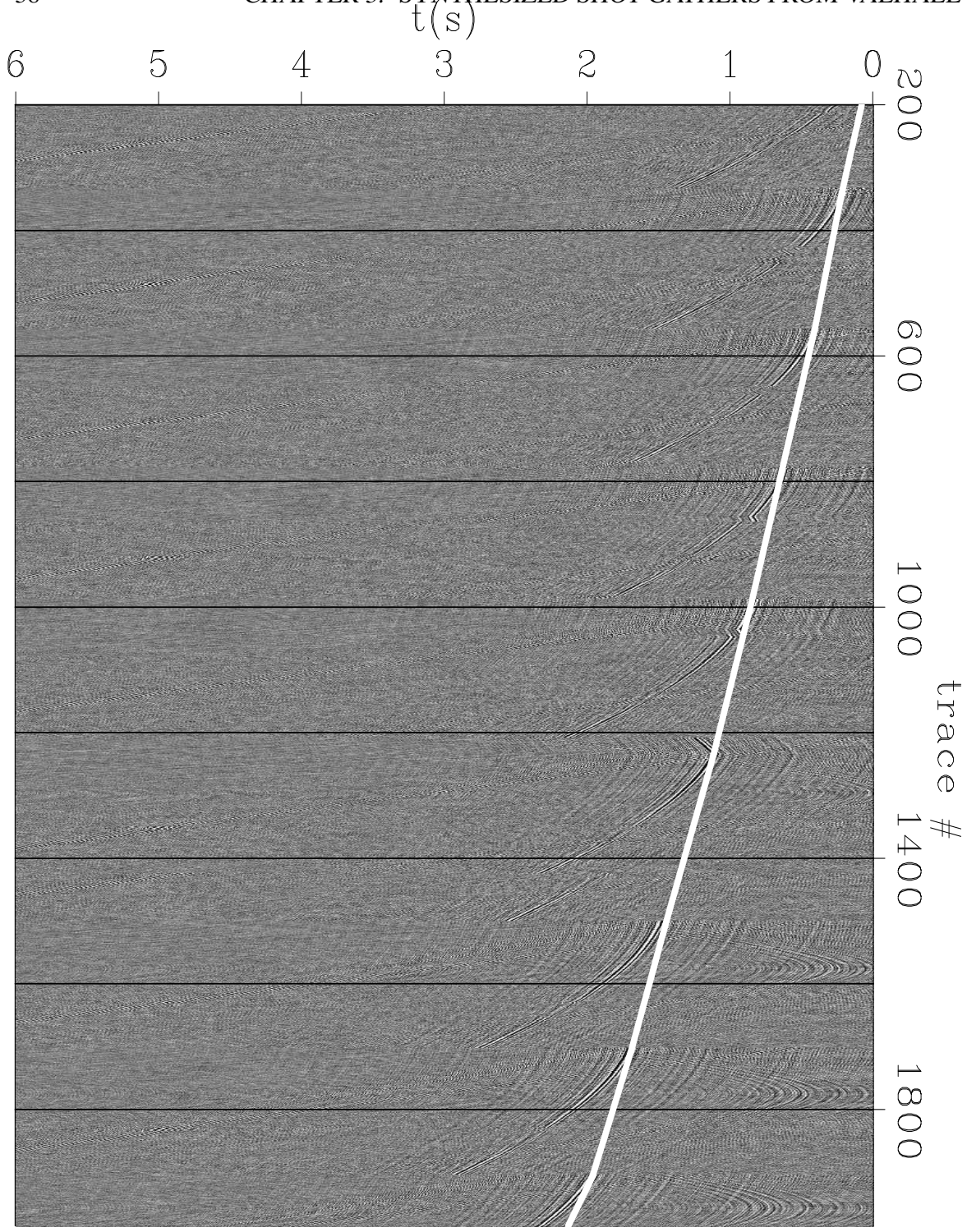

Figure 3.9: Trace-by-trace spectral whitening applied to shot-gather in Figure 3.7. Line connecting minimum traveltimes almost perfectly straight. TimeShot-dec [CR]

orientation of the array, Figure 3.2, the source of energy should be somewhere S. West of the array toward the English coast.

The fact that the event does not contain the center of the hyperbola, proves that processing by correlation to produce conventional shot-gathers has failed. Specifically the requirement to sum the correlations from many shots in equation 1.1 has not been honored. If only a single impulsive subsurface source is captured by a passively recording array, correlation simply shifts the event up such that it arrives at $t = 0$ at the master trace used to create the gather. The panels in Figure 3.10 all show four lines (receiver locations marked with circles in Figure 3.6) from the array from the same correlated shot-gather in Figure 3.9. The panels were produced with data from the four time intervals into which the raw data volume was divided. Panel c is a subset of the gather shown in Figure 3.9. Each trace was correlated with the first trace in the panel. Thus the event on the autocorrelated trace is at time zero. Some of the character of the panels changes, but the presence and kinematics of the strong event is the same. The last panel was computed with data recorded almost one year after the data used in the first three panels.

Figure 3.11 shows four synthesized shot-gathers using data shown in the previous section investigating the character of the raw recordings. The master trace used for correlation in all panels was the first trace on North end of line 2 (trace 118). All panels use the deconvolutional variant of correlation described by equation 3.2 and show the Eastern half of the array. Only 12 s of passive data was used to produce all the results in the figure. Panel a shows the first three seconds of the causal lags using the data shown in Figure 3.4, which showed the ringing noise-train. No strong events are present, but there are some faint ringing hyperbolas described by water velocity.

Correlation, to first order, subtracts the initial time to the direct arrival in the master trace from all the other traces in the gather. The beginning of the noise-train in Figure 3.4 on the first trace (number 118), is at about 3.5 s. The top of the noise train on the last receiver line (trace number 2150) is at about 2 s. The complicated coda evident in the raw data should collapse to a simple wavelet during correlation. Therefore, we expect the top of the energy on the last receiver line to lie at about -1.5 s. Figure 3.11b contains the acausal lags associated with the correlations presented in panel a. The water velocity event overlain on the traces has

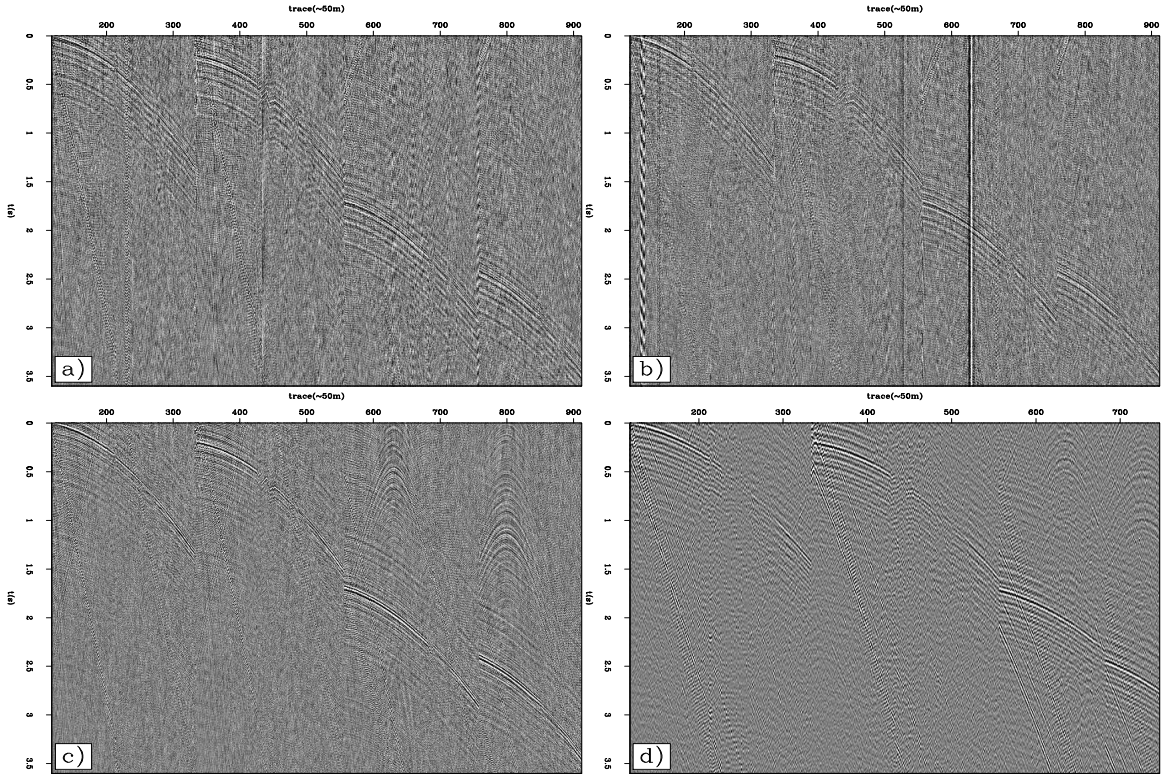

Figure 3.10: Ubiquitous strong event in deconvolved shot-gathers from data recorded 9 hours (b), 25 hours (c), and 11 months (d) after that used to produce the panel a. The third panel is a subset of the gather shown in Figure 3.9. TimeShot-event [CR]

a clear minimum on the last hyperbola at -1.5 s, which is exactly what is to be expected for the single-source scenario just described. The hyperbola under the overlays rings to the bottom ($t = 0$) of the panel. Given the long (7 s) coda of the noise train in the input, these are probably correlation side lobes. The side lobes continue past $t = 0$ and on to panel a.

The bottom row of Figure 3.11 are the deconvolved correlated gathers using trace 118 as the master trace, and the raw data from Figures 3.3 & Figure 3.5 respectively. In each case only 12 s of data was correlated. Faint hyperbolas are discernible in the early time of the right side of panel d. The faint hyperbolas have the same kinematic description as the water velocity events in panel b and Figure 3.5. The most obvious energy however is in the events similar to the strong arrivals in Figure 3.9 and Figure 3.10.

Correlation masks some of the characteristics of the source energy. The source could be impulsive or a long sweep containing many frequency components like a vibrator source. The latter seems less likely. The source could be a single strong event, or many similar repeated events with low amplitude. Given the presence of the event during all the time intervals in Figure 3.10 (spanning 1 year), I favor the latter explanation. I believe the energy is localized in space, and ubiquitous in time. The fact that the event is clear after correlating 12 s or 9 hours of raw data means that the source must be fairly powerful. The extended noise-train in the data shown in Figure 3.4 used to synthesize the gathers shown in Figure 3.11a,b indicates that over short time intervals, local cultural noise can overpower the temporally stable event revealed in Figures 3.10a-d.

Figure 3.12 is the frequency-wavenumber power spectrum of the raw data from a line of receivers. The frequency axis has been windowed to 23 Hz to avoid Frequency domain wrap-around of steep linear events characterized by water velocity slope. Two energy trains are observable on either side of zero on the wavenumber axis that could be subsurface signal. Panel b has been muted to preserve the energy near zero wavenumber and discard the strong planar water velocity energy. This Fourier domain mute was applied to 100 minutes of raw passive data before correlation to investigate the steeply dipping (fast) energy near the center of the panels.

Figure 3.13 shows a shot gather produced from the data preprocessed with the Fourier

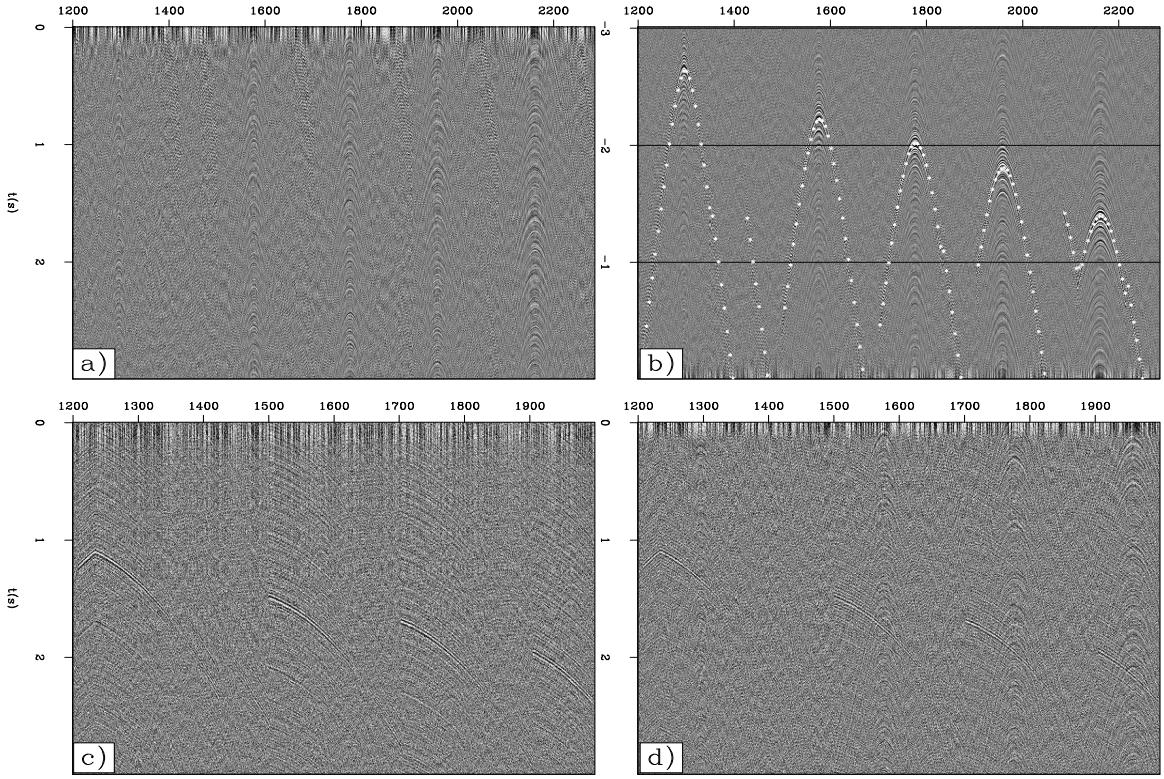

Figure 3.11: Correlated gathers from the Eastern side of the array. Top row: Early causal (a) and acausal lags (b) of a correlated gather using the data in Figure 3.4. Overlays on panel a have the same velocity (1450 m/s) and origin as those delineating the top and bottom boundaries of the noise train in the raw data. Bottom row: Early causal lags of correlated gathers using 12 s of raw data. Panel c used data in Figure 3.3 and panel d used data in Figure 3.5. TimeShot-evtest [CR]

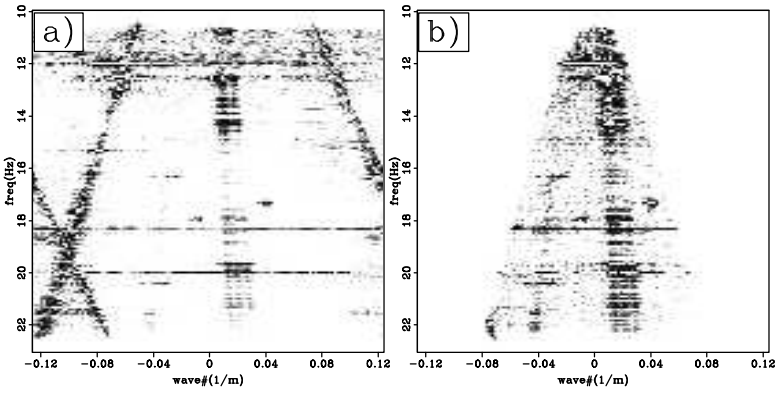

Figure 3.12: Frequency-wavenumber power spectrum of on OBC cable calculated from raw passive data. Panel b shows mute applied to focus on energy near zero wavenumber. TimeShot-fkpow [ER]

domain mute in Figure 3.12b). A single strong event is apparent. It is aliased and has much lower frequency content that the event in Figure 3.9. It is however the same event. This proves that the kinematics of the distant event have sufficient curvature in the inline direction that a FK-mute of slow linear events does not remove the energy.

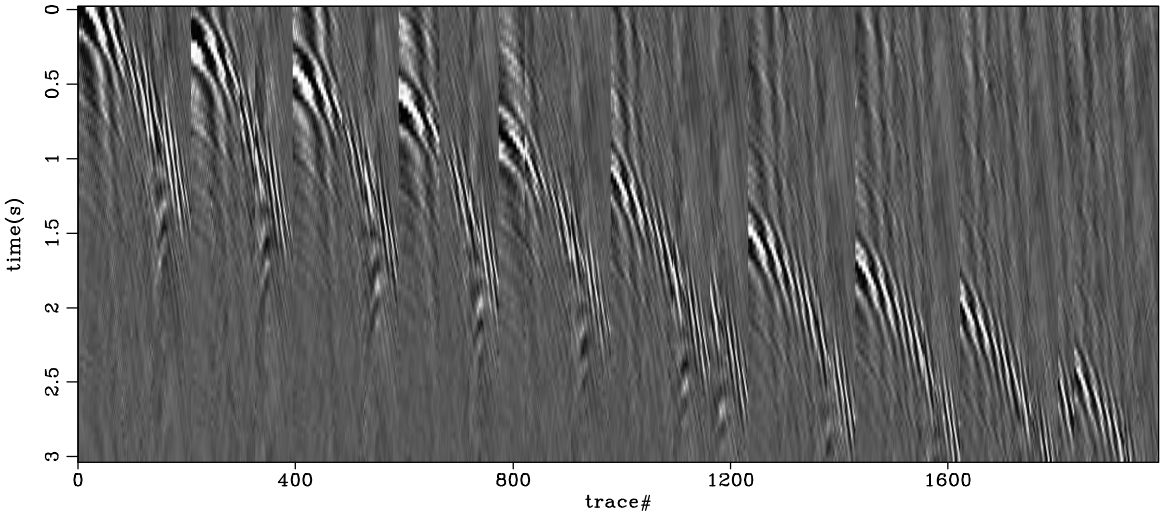

Figure 3.13: Correlated shot gather synthesized from passive data after preprocessing with the Fourier domain mute shown in Figure 3.12. TimeShot-fkgath [ER]

SOURCE IDENTIFICATION

Figure 3.14 shows the same correlated gathers as Figure 3.10. Superimposed on the data are time picks auto-picked by amplitude. The picks are not very accurate due to the effort required to maintain continuity. These picks, and the receiver locations, are the data used to invert for the source location that caused these events. The forward model used for the inversion was the kinematics of a reflection from an arbitrary plane. Inversions for a direct arrival from depth were not successful.

The equation describing the traveltime of a planar reflection in shot-receiver coordinates is

$$v^2 t^2 = \mathbf{x}^2 + 4z^2 + 4z\mathbf{x}\cos\alpha\sin\phi\ , \tag{3.3}$$

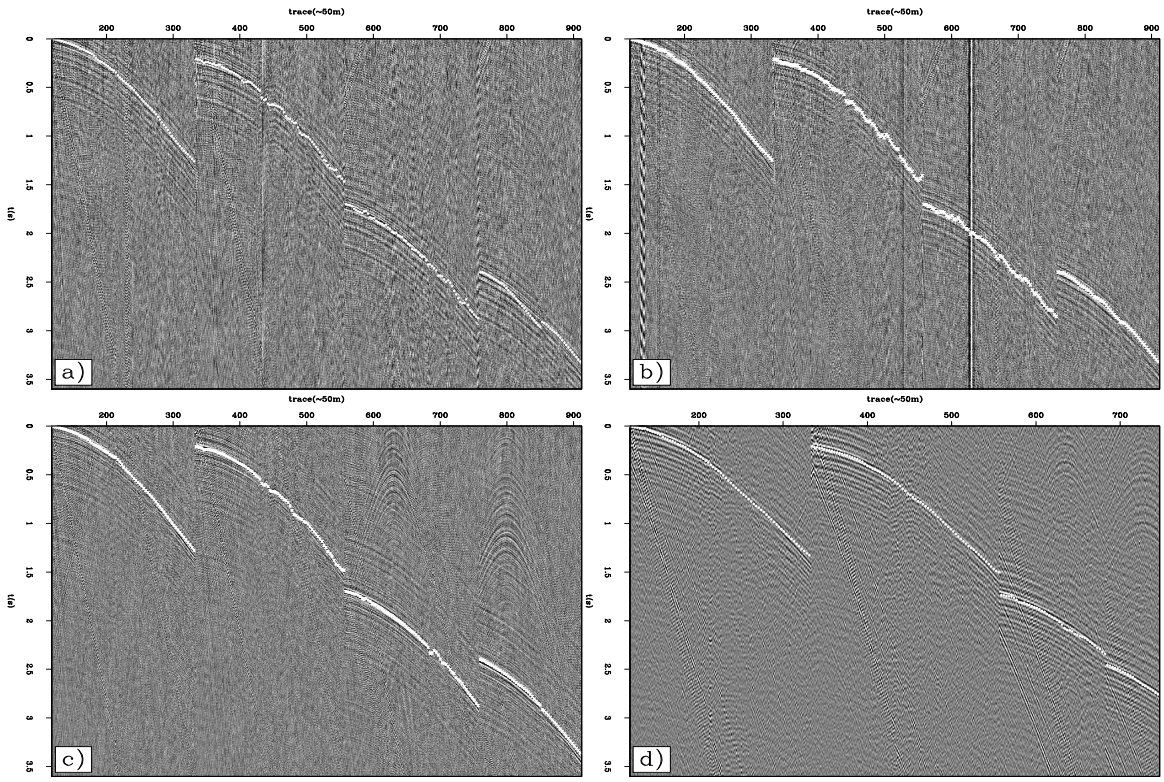

Figure 3.14: Auto-picked time values along event in correlated gathers. Picks are used as data to invert for the source location. TimeShot-picks [CR]

where $\mathbf{x}$ is the horizontal distance from the source to the receiver, z is the depth to the reflector under the source location, α is the dip direction of the plane, and ϕ is the dip of the plane. At the limit of $z = 0$, the operator solves for a co-planar direct arrival. Correlating data with a single master trace subtracts the time to the source trace from each trace in a gather. Therefore, the forward modeling operator used in the inversion solves for the time to every receiver, and then subtracts the time, t_s, to the master trace used for correlation. This calculates the time differences produced in a correlated panel. Subtracting t_s in the forward modeling operator greatly diminishes the operator's sensitivity to the terms on the RHS involving depth. Also, large horizontal distance will result in the first term, $\mathbf{x}^2$, to dominate the others. The inversion technique used was a micro-genetic algorithm (Krishnakumar, 1989). The model space was defined as the ensemble: Average velocity through which the rays have passed, areal location of the source, and orientation angles and depth of the reflection plane. The best results were obtained using the l^2 norm to evaluate the power of the data fitness function.

The panels in Figure 3.15 show the effectiveness and quality of the inversion results. The genetic algorithm uses a seed number that determines the characteristics of the first population as well as how the future generations change. I used fifteen seed numbers to begin inversions with the synthesized shot gathers from each of the four subdivisions of the passive data. Figure 3.15 is a representative sample of the inversion results from the four volumes of synthesized shot gathers. The panels in the figure show the convergence of the inversion. The total convergence of the inversion is shown in panel a. The convergence of the model parameters velocity, distance East, and distance North (respectively) to specific values is shown in panels b-d. In each case the vertical axis is the fitness value that the inversion is minimizing. The relative width of the data cloud at the minimum fitness value for the 3 model parameters shown reflects the model precision of the inversion for this data. Velocity and distance North are very well constrained, but distance East has a wide region of minimum energy. Not shown are the plots for the model parameters associated with the planar reflection: depth, dip, and azimuth. These parameters were completely within the null space of the inversion.

Figure 3.16 shows the forward modeled time picks from the inversions over a synthesized shot gather. The best model parameters from all 15 inversions are forward modeled and plotted. The points are very precise in picking even minor deviations from regularity in the array

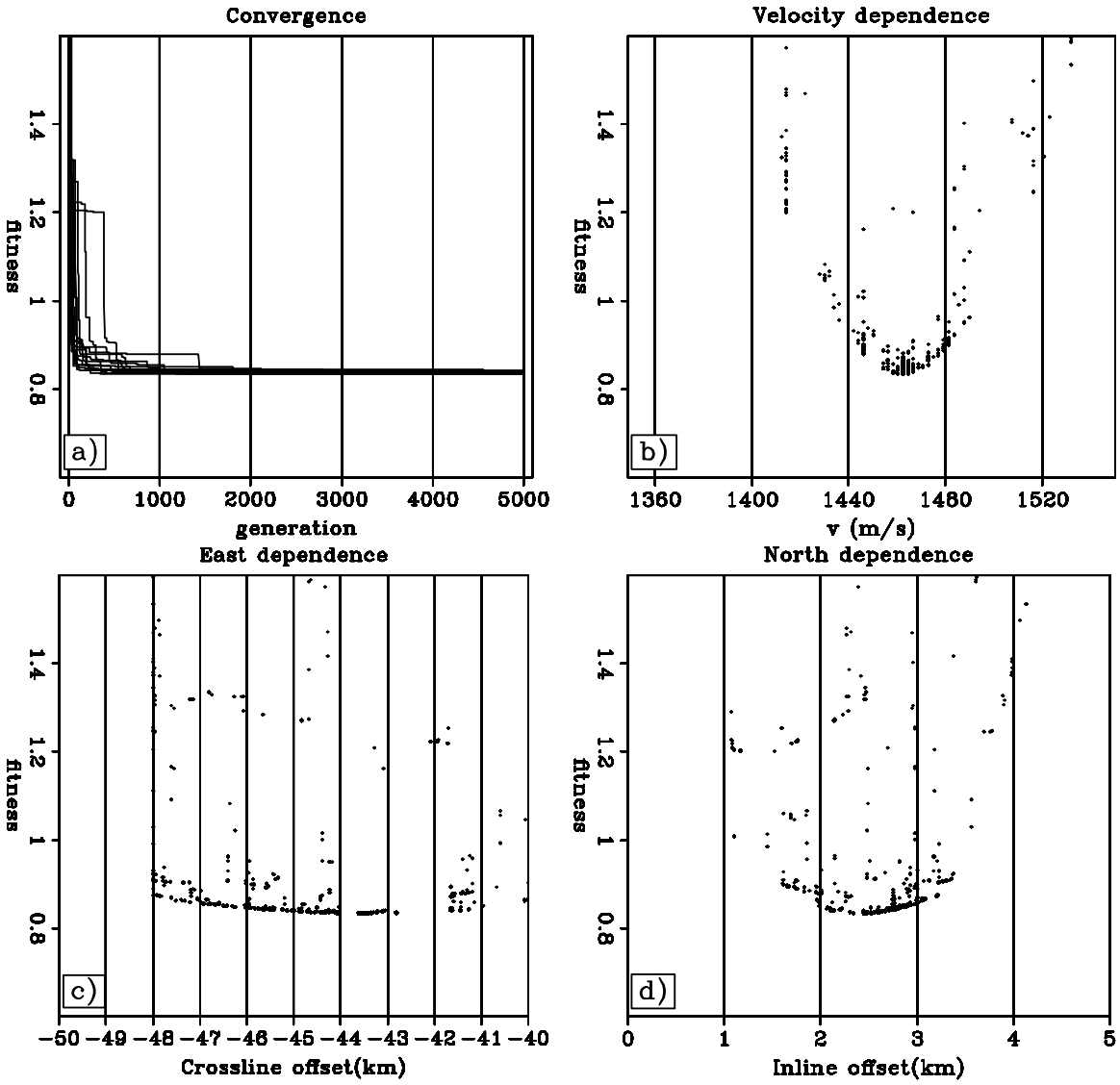

Figure 3.15: Residual energy of the inversion to locate the source of the energy causing the event in Figure 3.14. As the inversion iterates, overall residual energy decreases, and the standard deviation of the model parameters diminishes for well constrained members. TimeShot-inv [CR]

geometry and are much better at describing the event than the auto-picks in Figure 3.14. The quality difference between the picks that went into the inversion and the result account for the residual energy in Figure 3.15a. The inversion was not able to match the bad data (imprecised picks) because it was required to honor equation 3.3. Therefore, the result is not able to converge to zero.

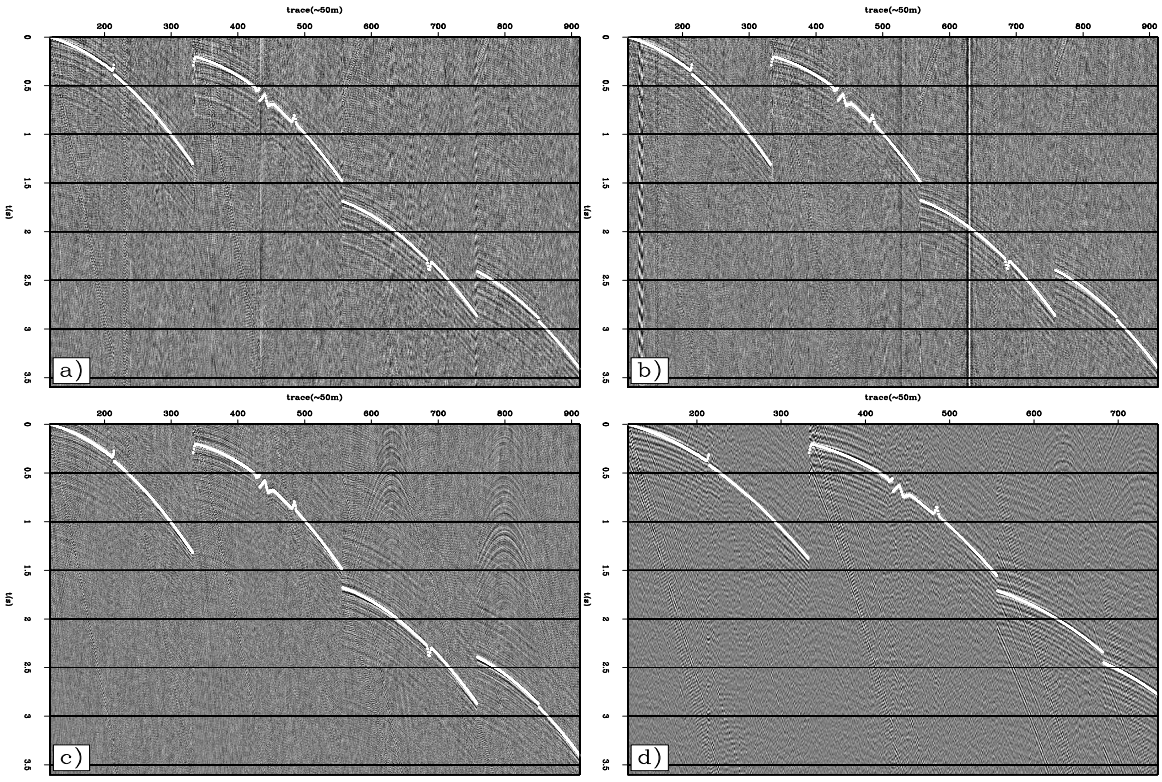

Figure 3.16: The forward modeled time picks from 15 inversions are plotted over each panel in Figure 3.10. The accuracy of the times is very faithful to the irregularities in the array layout in contrast to the auto-picked data input to the inversion, Figure 3.14. TimeShot-mods [CR]

I selected values for map coordinates and velocity at the location of the minimum from all 15 inversions using graphs such as those shown in Figure 3.15b-d. The best velocity for the three data sets from 2004 was $\sim$ 1455 m/s, and 1440 m/s for the data from 2005 which are appropriate for compressional waves in the water column. The (x, y) locations measured as distance from the NW corner of the array in kilometers were: (2.5,-44.0), (2.0,-40.0), (2.4,-43.5), (2.75,-43.5) in the rotated local coordinate system shown in Figure 3.6. Because the

inversion returned very reliable water velocities in all cases, the lack of sensitivity for the subsurface parameters is mitigated. If the event must be in the water column, the sea surface and floor are the only potential reflectors. Since the receivers are on the sea floor, the most simple explanation of these results is that the source is also at the sea floor and reflects from the sea surface once before arriving at the array. However, at such large horizontal offset, and shallow water column, the forward model cannot distinguish between this model and the direct arrival from the surface to the sea floor. Conversely, the source could be at the array, travel roughly horizontally, and reflect back from a nearly vertical object. The latter situation is not plausible, nor is the direct arrival associated with this model recorded by the array. From these results, I interpret the energy to arrive in a direct path through the sea to the array. The data do not allow locating the source at the sea surface or the sea floor.

I used the mathematic description of the direct arrival from the distant source to design a stacking operator. Summing along the tragectory of the arrival at all times in the raw data returns a measure of the energy in the data associated with this event. I also summed the energy in the raw data volumes associated with zero ray parameter. The horizontal plane wave sum was consistantly at least two orders of magnitude less than the value returned by the stacking operator designed with equation 3.3 and the parameters calculated by inversion. Similar partitions of energy were observed in the summations using the synthesized gathers instead of raw data.

Using the velocity and location values calculated by the inversion, I forward modeled time picks at every receiver station for use as data in an exhaustive search over location variables. Figure 3.17 shows the results of the search using the four time sections of passive recordings. The gray scale shows the inverse of the total data misfit normalized by the maximum value. The same line is plotted on the panels for reference (8^o from the horizontal axis). All data volumes resolve the source location at similar locations with very similar trends in precision. A request to the Norwegian Petroleum Directorate indicates that there were no active seismic vessels acquiring data in this region on or around February 15, 2004. The similar location derived from the data collected in 2005 indicates that surface seismic acquisition is likely not the cause of this feature.

Figure 3.18 is a detailed map of the Norwegian and British oil infrastructure around the

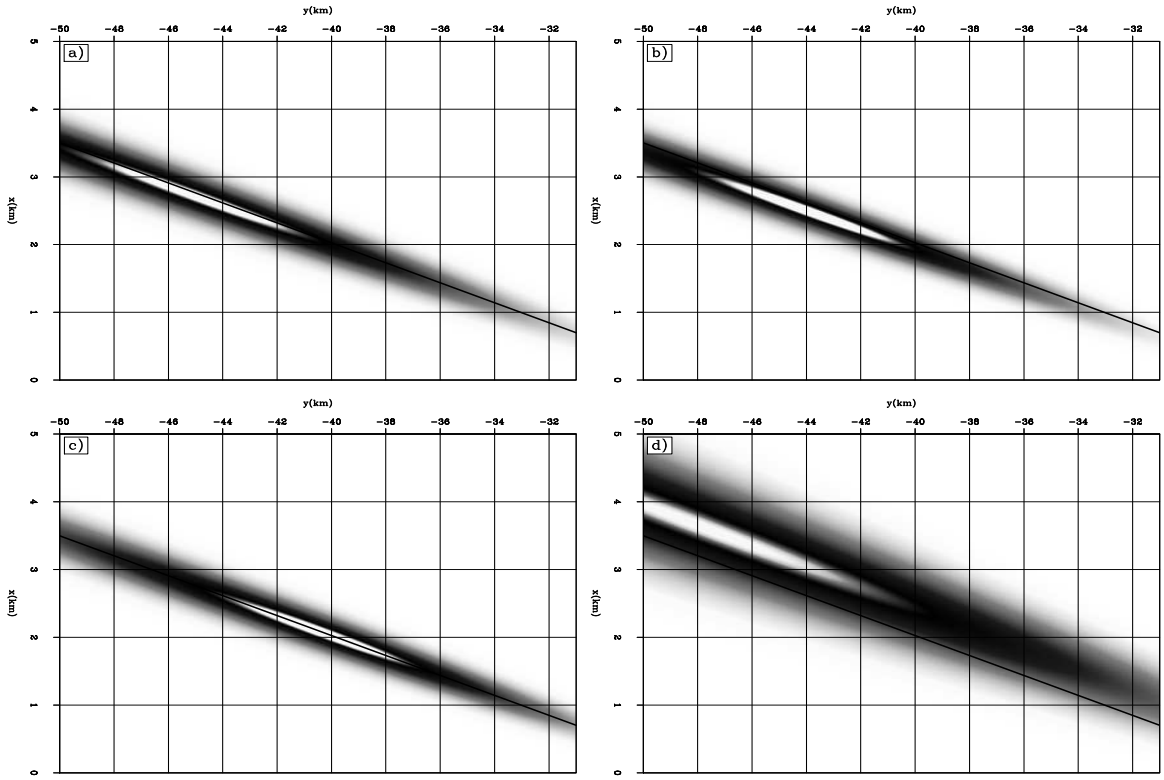

Figure 3.17: Sensitivity to horizontal location for the inversions using the four periods of passive data. TimeShot-xy [CR]

Valhall reservoir. Also plotted are the footprint of the receiver array (gray rectangle), and the location of the trace used as the virtual source function (push-pin icon G118) for the gathers presented above. Superimposed as a flat image (and thereby introducing small projection errors) is a map of the British production facilities in the area. The black line from the receiver array ends in the SW at the locus of the energy provided by the inversions described above. The location of the source for the events in Figure 3.10 is exactly over the Ardmore field in British controlled section of the North Sea. The British Department of Trade and Industry [3]

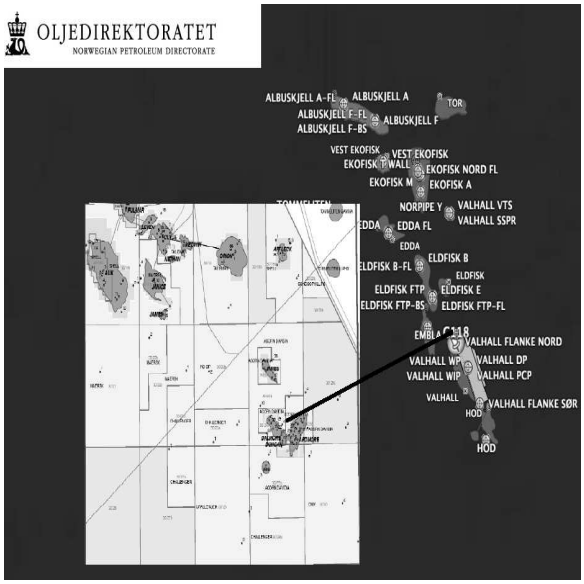

Figure 3.18: A small section of the British infrastructure map, the Norwegian infrastructure, and the location of the energy source inverted in Figure 3.17. The inverted locus of the energy in the gathers (the SW terminus of the black line) corresponds exactly to the location of the Ardmore development. TimeShot-mapa [NR]

describes the Ardmore development. It differs from the Valhall operation in several important ways. The Ardmore facility has no permanent structures, nor is it connected to an export pipeline. Instead, two vessels are permanently moored over the field: One contains production facilities, the other is used to store liquids for periodic transport to shore. This operation has no way to handle produced gas and must therefore flare all produced gas.

CONCLUSIONS

The energy responsible for the features in the raw data, Figures 3.4 - 3.5, are likely related as they share a locus at the production facilities within the array and are both characterized by

[3] www.og.dti.gov.uk/environment/permits/TuscanArdmore.htm

water velocity. I suspect that the noise-train in Figure 3.4 is a collection of aliased repeating events similar that found in Figure 3.5. Also, the gathers generated with data showing the diffuse noise-train, Figure 3.4, have almost identical kinematics to the raw data showing a crisp water-velocity event, Figure 3.5. It is possible that some activity on the platforms could sometimes be impulsive in nature or more drawn out. In either case, the correlated gathers do not show convincing evidence that the energy penetrates the subsurface after the direct arrival is recorded. Forward modeling a direct arrival to the receiver stations shows that water velocity events are aliased close to the source with this array. This analysis of the raw data also shows that the predominance of observable energy shares a single source location.

Correlating the raw data to produce synthesized shot gathers was always performed on 12 second records. These individual results were summed from 1-2500 times to generate some approximation to active seismic shot gathers in accordance with the theory of interferometric imaging. The gathers produced with a single 12 second record, Figure 3.11, or 15 hours of data correlated in 12 second sections, Figure 3.10, show an identical strong event with velocity 1450 m/s arriving from the Ardmore field 40 km to WSW.

It seems counter-factual to attribute the source of this energy to a distant production operation when major production, drilling, and injection activities within the array have not generated events that match the power and bandwidth of this most obvious arrival. Gas flaring at Ardmore is the most significant difference between the two operations. I believe that the gas flare is the energy source for the strong off-array event revealed by whitened correlation processing. Synthesized shot gathers produced with short, 12 s, time windows of raw data show very different results depending on the character of the raw data used. Figure 3.11 shows that when there are high levels of local energy generated by the Valhall production facilities, synthesize gathers produced with short time windows do not produce the far-field production event. Otherwise, the far-field production energy dominates the correlation result using raw data windows as short as 12 s and as long as 9 hours.

The synthesized gathers produced with 36 hours of passive recordings do not provided subsurface information. The gathers are dominated by a cultural noise source. The energy within this noise is several orders of magnitude stronger than anything else in the data. The strength and continued presence of this energy makes it very difficult to remove or ignore.